

Article

Effect of Cavitation Intensity on the Cavitation Erosion Behavior of 316L Stainless Steel in 3.5 wt.% NaCl Solution

Jiaxiu Hu ^{1,2}, Lianmin Zhang ^{2,*}, Aili Ma ², Pingli Mao ^{1,*} and Yugui Zheng ²

¹ School of Materials Science and Engineering, Shenyang University of Technology, Shenyang 110870, China; jxhu@imr.ac.cn

² CAS Key Laboratory of Nuclear Materials and Safety Assessment, Institute of Metal Research, Chinese Academy of Sciences, 62 Wencui Road, Shenyang 110016, China; alma@imr.ac.cn (A.M.); ygzhen@imr.ac.cn (Y.Z.)

* Correspondence: lmzhang14s@imr.ac.cn (L.Z.); pinglimao@yahoo.com (P.M.)

Abstract: In this study, the cavitation erosion behavior of 316L stainless steel under different cavitation intensities in 3.5 wt.% NaCl solution was investigated with scanning electron microscopy and various electrochemical tests. Results indicated that cavitation intensity corresponding to CE amplitude of 5 μm was lower than that of the mechanical bearing capacity of passive films. When subjected to cavitation erosion (CE), Open circuit potential (OCP) shifted to the noble direction instantaneously, which was mainly attributed to enhanced oxygen transfer of the cathode due to stirring effects of CE. By contrast, high cavitation intensities corresponding to CE amplitudes of 25 μm and 55 μm exceeded the mechanical bearing capacity of passive films, causing significantly reduced OCP associated with metal dissolution of the anode from mechanical damage. Potentiostatic polarization and Mott–Schottky tests showed that 316L SS subjected to low cavitation intensities displayed good repassivation properties. However, repassivation performance was markedly weakened when high cavitation intensity was applied, resulting in weaker protection of the passive films with high carrier density.

Keywords: 316L stainless steel; cavitation erosion; cavitation intensity; passive films; repassivation property



Citation: Hu, J.; Zhang, L.; Ma, A.; Mao, P.; Zheng, Y. Effect of Cavitation Intensity on the Cavitation Erosion Behavior of 316L Stainless Steel in 3.5 wt.% NaCl Solution. *Metals* **2022**, *12*, 198. <https://doi.org/10.3390/met12020198>

Academic Editor: Evgeny A. Kolubaev

Received: 28 December 2021

Accepted: 17 January 2022

Published: 21 January 2022

Publisher's Note: MDPI stays neutral with regard to jurisdictional claims in published maps and institutional affiliations.



Copyright: © 2022 by the authors. Licensee MDPI, Basel, Switzerland. This article is an open access article distributed under the terms and conditions of the Creative Commons Attribution (CC BY) license (<https://creativecommons.org/licenses/by/4.0/>).

1. Introduction

Cavitation erosion (CE) is a common damage form relative to pumps, turbines, propellers, valves and other flow passage components in both corrosive media (e.g., sodium chloride solution) and noncorrosive media (e.g., distilled water) [1–5]. Due to stirring effects of cavitation, the mass transfer process of electrochemical corrosion of materials was accelerated [6–9]. At the same time, shock waves and micro jets generated by the collapse of cavitation bubbles can cause significant plastic deformation of the materials of a flow passage component, thereby changing electrochemical activities of materials [10,11]. Passivation metals (e.g., stainless steels, titanium alloys and nickel alloys) usually possess superior corrosion-resistant performance, spontaneously forming dense, stable and protective passive films on their surfaces, consequently exhibiting high chemical stabilities in various corrosive media [12–16]. Passivation metals also have good repassivation performance, meaning that they can carry out repassivation self-repair when their surfaces are damaged, improving service performance in corrosive media [17–20]. Consequently, passivation metals, especially stainless steels, are widely used in aerospace, nuclear energy, marine and other industrial fields, particularly in the presence of CE, due to their superior corrosion resistance and good mechanical properties [21–25].

Influence of CE on passive film stability has always been a focal point of CE research. In the area of research on stainless steels, electrochemical methods are frequently used to monitor repassivation and depassivation processes. Zhang et al. studied the effect of CE

on electrochemical corrosion behavior of austenitic stainless steel by conducting potentiodynamic polarization. It was found that CE significantly accelerated oxygen transfers of the cathode in addition to obvious current oscillation in the anodic passivation region, implying that passive films were in a metastable state under CE [26]. Luo et al. adopted an alternating CE–quiescence method to investigate the potential change of CrMnN duplex stainless steel in NaCl solution. Results indicated corrosion potentials shifted negatively under CE, demonstrating that CE with high cavitation intensity destroyed the integrity of passive films instantaneously, with obvious repassivation behavior observed once CE stopped [27]. Kwok et al. studied changes of corrosion potential in 316L and 304 stainless steels over time in 3.5 wt.% NaCl solution and found that CE moved corrosion potentials toward the direction of active dissolution. Passive films on the materials were initially destroyed as CE was switched on, and then the materials were repassivated rapidly. When CE stabilized, the stainless steel surfaces were covered with a passive film thinner than the original, with uniform thicknesses of 2–3 nm while simultaneously exhibiting weak protective properties [28]. However, the cavitation intensity selected in the aforementioned research was relatively high, exceeding the mechanical bearing capacity of the passive films; thus, the electrochemical behavior observed is limited to stainless steels under high cavitation intensities. In actual service conditions, the cavitation intensity is usually low and fluctuates within a certain range. Therefore, selecting an appropriate cavitation intensity range to study CE behavior is of more significance for understanding CE damage mechanisms in stainless steels.

In this study, the CE behavior of 316L stainless steel (316L SS) under different cavitation intensities in 3.5 wt.% NaCl solution was investigated. OCP was adopted to monitor potential changes under alternating CE and quiescent states. Meanwhile, potentiostatic polarization was used to assess the effect of alternating states of CE and quiescence on cathodic and anodic reactions of 316L SS. Mott–Schottky tests were also conducted to evaluate passive film stability. Additionally, surface morphology observation was carried out for specimens subject to different cavitation intensities. This study provides some important insights into understanding CE damage mechanisms in 316L SS subjected to different cavitation intensities.

2. Experiment

Solution-annealed 316L SS (heated at 1050 °C for 1 h and then quenched in water) was selected as the experimental material due to its superior corrosion resistance and good mechanical properties [29–31]. The chemical composition of 316L SS used in the experiment is shown in Table 1, and the dimensions of the CE samples are displayed in Figure 1. All CE specimens were ground by 400-grit, 1000-grit and 2000-grit sandpapers in sequence; then, they were polished using diamond grinding paste with a particle diameter of 0.5 µm. Ultrasonic CE equipment made by Nanjing Xian Ou Instrument Manufacturing Co., Ltd, Nanjing, China. was used for the CE tests, as shown in Figure 2, and the working temperature was maintained at 25 ± 2 °C using a temperature control box. The horn tip was held at a depth of 15 mm in 3.5 wt.% NaCl solution, and the CE specimen was placed co-axially with the horn fixed a distance of 1 mm from the horn tip. CE tests were performed according to ASTM Standard G32-10 [32]. Detailed parameters can be obtained from our previous research studies [27,33].

Table 1. Chemical composition (wt.%) of 316L SS used in the experiment.

Elements	C	Si	Mn	P	S	Ni	Cr	Mo	Ti	Fe
wt.%	0.02	0.68	1.37	0.01	0.001	12.2	17.5	2.61	0.68	Bal.

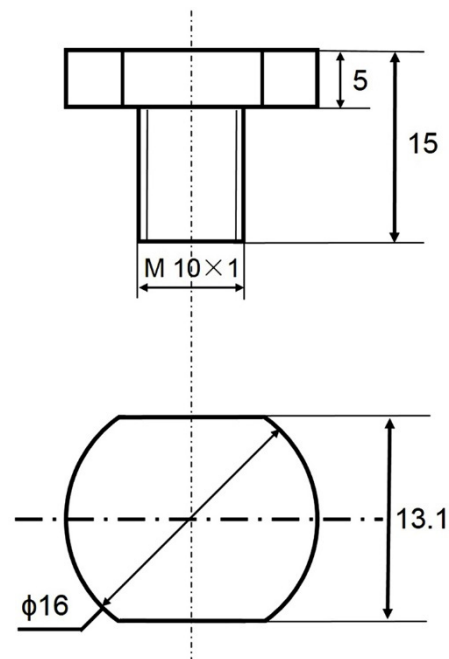


Figure 1. Dimensions of CE samples (unit: mm).

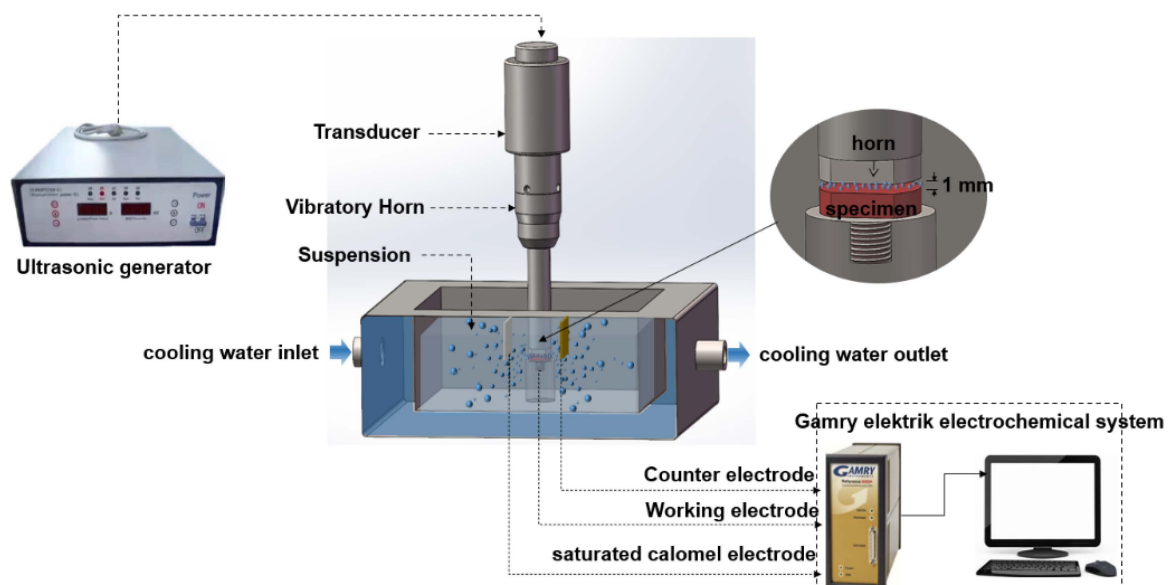


Figure 2. Schematic diagram of CE equipment with electrochemical test system.

Electrochemical tests adopted a traditional three-electrode electrochemical measurement system, a platinum plate as the counter electrode and a saturated calomel electrode (SCE) as the reference electrode with the sample as the working electrode. The surface area of the working electrode (the surface subject to CE) was 1 cm^2 . Prior to electrochemical tests, the samples were sealed using epoxy resin; then, working surfaces were wet-ground and polished with the same procedure as the CE specimens. Cavitation intensities can be adjusted by changing the amplitude of CE; the CE amplitudes selected were $5 \text{ }\mu\text{m}$, $25 \text{ }\mu\text{m}$ and $55 \text{ }\mu\text{m}$, corresponding to the powers of 8 W , 20 W and 36 W , respectively. Open circuit potential (OCP) was measured under alternating CE and quiescence states, with a dwelling time of 300 s each. Potentiodynamic polarization tests were carried out at a scanning rate of 0.5 mV/s from -0.3 V versus OCP to 0.6 V versus SCE under different cavitation intensities. Potentiostatic polarization measurements were conducted at 0 V

versus OCP under alternating quiescence and CE states with different cavitation intensities. Mott–Schottky measurements were also performed to evaluate the stability of passive films formed on working surfaces under different cavitation intensities at a scanning rate of 20 mV/s, with a scanning range from $-0.5 V_{SCE}$ to $0.4 V_{SCE}$ and testing frequency of 1000 Hz. In order to ensure the accuracy of data, all electrochemical tests were conducted three times. Additionally, surface morphologies of CE samples subject to different cavitation intensities were characterized by scanning electron microscope (SEM, INSPECT F50) made by FEI Eletron Optics B.V., Eindhoven, Netherlands.

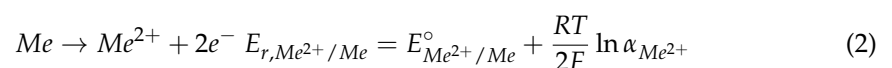
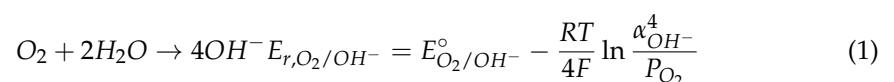
3. Results and Discussion

3.1. CE Damage Morphologies with Different Cavitation Intensities

Figure 3 shows CE morphologies of 316L SS subject to CE amplitudes of 5 μm , 25 μm and 55 μm . After 2 h with 5 μm CE amplitude, it is clear that 316L SS shows slight plastic deformation while the entire surface remains smooth. When CE amplitude increased to 25 μm , the surface of 316L SS presented obvious plastic deformation with many small bulges at grain boundaries noted after CE for 2 h, implying more serious surface damages. Furthermore, a large number of convexities were observed when the sample undergoes 2 h CE with an amplitude of 55 μm ; in particular, there exist obvious slip bands in the crystal, which is significantly different from cases with low CE amplitudes after the same CE time. Prolonging CE time to 4 h at 55 μm amplitude, obvious surface damage with many cracks at grain boundaries and slip bands appear, and a new surface after local spalling was also observed. During the CE process, dislocation accumulation due to plastic deformation usually occurs at grain boundaries or slip bands where microcracks will form as shear stress exceeds critical shear stress. The surface damage of stainless steels caused by CE is widely reported [34–40]. The evolution of surface damage morphology of stainless steels presents similar change trends, but the damage degree after the same CE time is significantly distinct between different stainless steels. Overall, CE morphologies corresponding to different amplitudes show obvious differences, with higher CE amplitudes resulting in more serious surface damage.

3.2. OCP Measurements under Alternating CE and CE States

In order to further clarify the effect of different CE amplitudes on OCP of 316L SS, OCP plots under alternating CE and quiescence states of 300 s dwelling times are shown in Figure 4. For each CE–quiescence cycle, significant OCP changes indicate different electrochemical correspondences. Due to low H^+ concentrations in neutral solutions, the hydrogen evolution reaction can be ignored. Therefore, fluctuations in potentials should be closely related to two competitive factors including an increase in mass transfer of oxygen (Equation (1)) and the destruction of passive films (Equation (2)) [41,42].



With a CE amplitude of 5 μm , Figure 4b shows that each CE–quiescence cycle includes four stages. In stage 1, OCP changes from -186.6 mV to -159.7 mV, proceeding toward the noble direction when CE is switched on. In this situation, increased mass transfer of oxygen caused by CE accelerates the cathodic reaction of oxygen reduction. Meanwhile, the passive films formed on the sample's surface maintain integrity at low cavitation intensity; thus, they are controlled by the cathodic reaction at this stage. In stage 2, OCP shows a negative shift reaching -168.7 mV. Since electrons consumed by the cathodic reaction are supplied by anodic metal oxidation, the increased cathodic reaction accelerates the anodic reaction to some extent, resulting in the negative shifts in potential. In stage 3, OCP is maintained in a relatively stable range from -169 mV to -164 mV, indicating that the cathodic and

anodic reactions achieved equilibrium. In stage 4, the potential rapidly shifts to the negative direction once CE is switched off, which should be attributed to a significantly reduced reaction rate of the cathode. Subsequently, the potential moves towards the noble direction slightly due to the regeneration of passive films, which cover the entire surface of 316L SS. Note that similar phenomena can be observed in each CE–quiescence cycle, and the change in OCP of each CE–quiescence cycle becomes smaller, which is possibly related to gradually increasing surface stress affecting the electrode reaction.

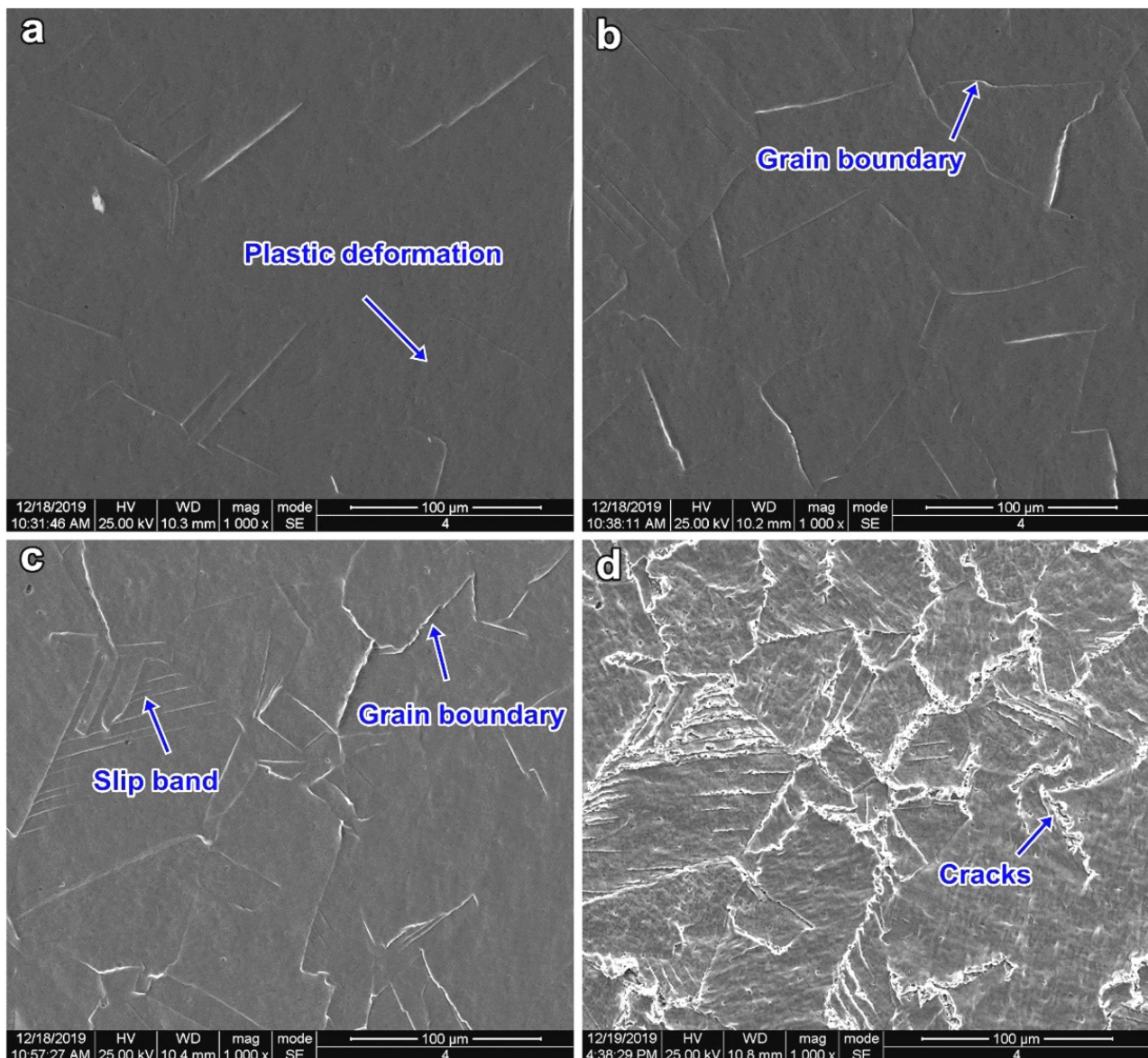


Figure 3. Surface morphologies of 316L SS with different amplitudes of CE: (a) 5 μm for 2 h CE, (b) 25 μm for 2 h CE, (c) 55 μm for 2 h CE and (d) 55 μm for 4 h CE.

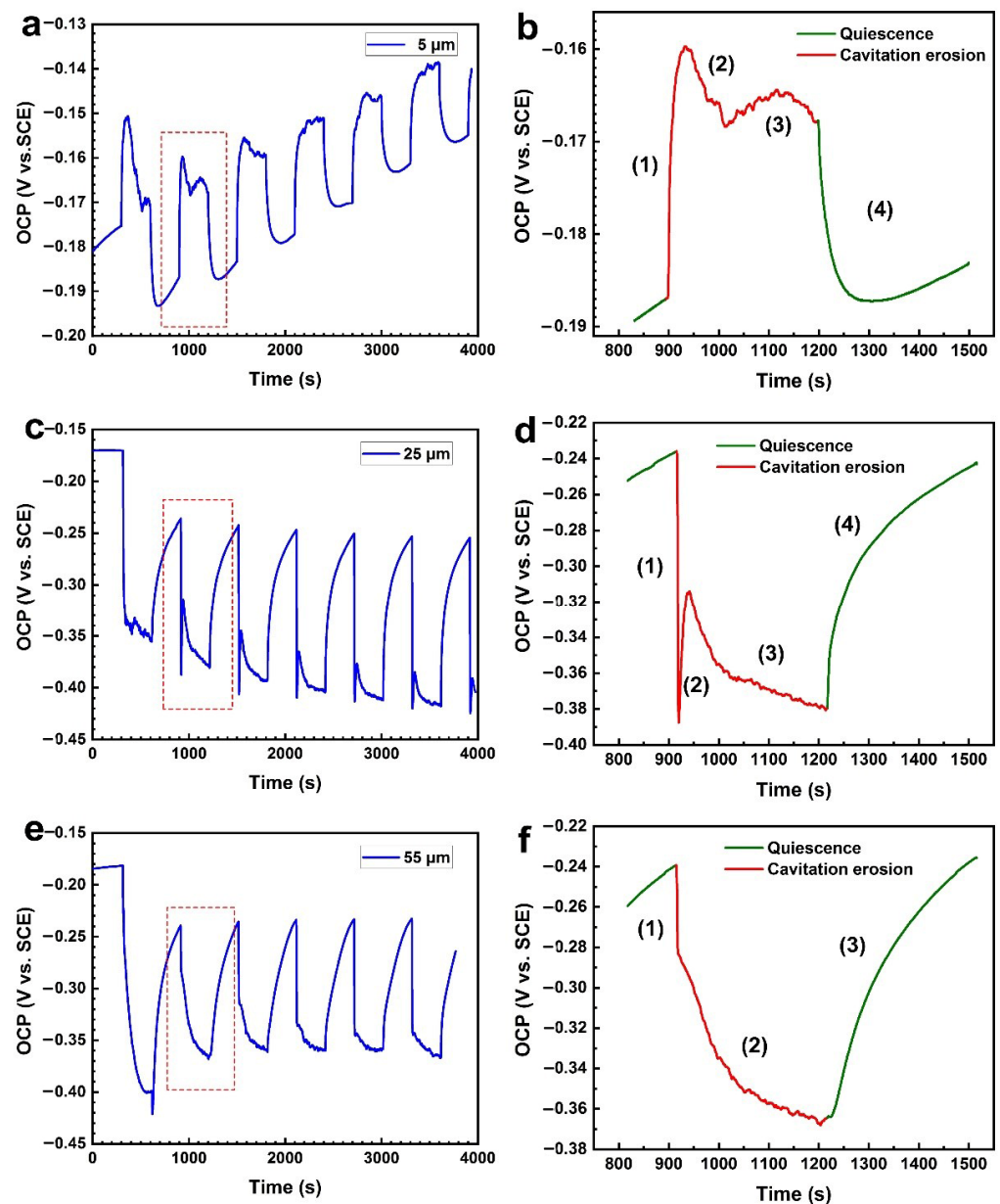


Figure 4. OCP of 316L SS under alternating CE and quiescence states of 300 s dwelling times with different CE amplitudes of (a,b) 5 μm , (c,d) 25 μm and (e,f) 55 μm .

Figure 4d shows alternating OCP under quiescence and CE of amplitude 25 μm ; here, there also exist four stages in each CE–quiescence cycle. Note that OCP moves rapidly in the negative direction when CE is switched on in stage 1 from -235.3 mV to -390.5 mV , which is significantly different from the case with an amplitude of 5 μm . It is clear that the passive films are destroyed instantaneously at this CE amplitude. In other words, the cavitation intensity corresponding to 25 μm amplitude exceeds the mechanical bearing capacity of passive films due to impacts of microjets and shock waves. As a result, the electrochemical process is controlled by the anodic reaction of metal dissolution due to the destruction of passive films. In stage 2, OCP moves positively to -311.9 mV and then proceeds negatively towards -366.7 mV ; this is as a result of mutual promotion between cathodic and anodic reactions, resulting in more serious damage relative to the passive films with the progress of CE. In stage 3, OCP maintains a relatively stable value at around -370 mV , but it depends on the balance between the anodic and cathodic reactions in later stages. In stage 4, OCP shifts quickly towards the noble direction when

CE is interrupted, a response closely correlated to the repassivation behavior of 316L SS. Although cavitation intensity is higher than mechanical bearing capacity of the passive films, 316L SS possesses superior repassivation properties and their passive films can be repaired in a short time; the repassivation process can cause a noble direction shift of potential dramatically. Additionally, the same phenomena can be observed in each CE–quiescence cycle. However, the change of OCP in each CE–quiescence cycle becomes larger due to the degradation of passive films or of repassivation performance, differing from the case with 5 μm CE amplitude.

An alternating OCP under quiescence and a higher amplitude CE of 55 μm is displayed in Figure 4e,f. OCP gradually decreases from -239.3 mV to -367.7 mV during the CE period, which is different from the case involving an amplitude of 25 μm . With a higher cavitation intensity corresponding to 55 μm amplitude, the passive films suffer more serious damage due to a higher cavitation intensity being compared to the mechanical bearing capacity of the passive films, making the anodic reaction dominant during the CE period (stage 1 and stage 2). Subsequently, OCP shifts quickly toward the noble direction when CE is switched off, exhibiting clear repassivation behavior similar to the case with an amplitude of 25 μm (stage 3). The destruction of the passive films is more serious after the CE period under a higher cavitation intensity, making it difficult to restore the integrity of the passive films to their initial states.

3.3. Potentiodynamic Polarization Tests under Different Cavitation Intensities

Figure 5a shows potentiodynamic polarization curves of 316L SS at different CE amplitudes, and the relevant fitting parameters are summarized in Table 2. According to the anodic polarization curves, the sample without CE (an amplitude of 0 μm) presents clear self-passivation behavior with a low corrosion current density (i_{corr}) of 0.406 $\mu\text{A}/\text{cm}^2$ while the anodic region displays a slight rightward shift under the CE state with 5 μm amplitude and an i_{corr} value of about 1.062 $\mu\text{A}/\text{cm}^2$. Meanwhile, the polarization curve displays an apparent passivation region without obvious current fluctuation. With an increase in CE amplitude to 25 μm , the anodic region shifts significantly to the right, and obvious current fluctuation is observed which may correspond to the local destruction of the passive films or pitting caused by CE. As the anodic part of the potentiodynamic polarization plot moves to the right, the largest i_{corr} of 4.045 $\mu\text{A}/\text{cm}^2$ was recorded, significantly higher than the case with 25 μm CE amplitude (2.959 $\mu\text{A}/\text{cm}^2$). Obviously, a larger cavitation intensity corresponding to 55 μm can cause more severe damage to 316L SS. In addition, it is easy to observe that oxygen transfer of the cathode is significantly accelerated when low cavitation intensity with 5 μm CE amplitude is applied. At the same time, with increased cavitation intensity by enhancing the CE amplitude to 25 μm , the cathodic reaction presents a slight increase compared with the case with 5 μm CE amplitude; a similar cathodic reaction is recorded with increased cavitation intensity corresponding to 55 μm CE amplitude.

Table 2. Fitting values of electrochemical parameters obtained from potentiodynamic polarization plots at different CE amplitudes.

Amplitude	E_{corr} (mV _{SCE})	i_{corr} ($\mu\text{A}/\text{cm}^2$)
0	-310.7	0.406
5 μm	-283.6	1.062
25 μm	-405.0	2.959
55 μm	-399.8	4.045

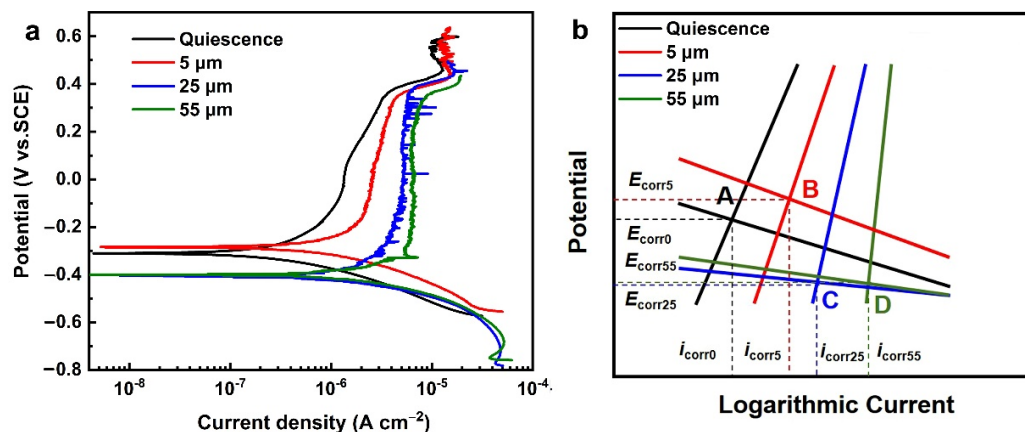


Figure 5. (a) Potentiodynamic polarization plots of 316L SS at different CE amplitudes. (b) Schematic diagram of ideal polarization curve of 316L SS at different CE amplitudes.

On the other hand, the corrosion potential (E_{corr}) also presents some differences at different CE amplitudes. The E_{corr} is about -310.7 mV at a static state (amplitude of 0 μm), and the value of E_{corr} becomes -283.6 mV at a CE amplitude of 5 μm; the values of E_{corr} reached 405.0 mV and 399.8 mV with the increase in CE amplitudes to 25 μm and 55 μm, respectively. The change of E_{corr} should be closely related to anodic and cathodic reactions, including both anodic metal dissolution and cathodic oxygen transfer. More specifically, E_{corr} is the equilibrium potential of cathodic and anodic reactions. Thus the ideal schematic polarization curves displayed in Figure 5b are adopted to explain changes in E_{corr} at different CE amplitudes. At a low CE amplitude of 5 μm, increases in cathodic reactions are more significant than that of the anodic reaction due to stirring effects caused by CE-accelerated oxygen transfer. The anodic reaction does not change markedly because the cavitation intensity corresponding to 5 μm CE amplitude is lower than that of mechanical bearing capacity of passive films, which display good protective performance. Thus, coupling cathodic and anodic reactions results in an improvement of E_{corr} (Point B in Figure 5b). With increased cavitation intensity corresponding to 25 μm CE amplitude, a contrasting change of the cathodic and the anodic reactions occurs in comparison to the case with 5 μm amplitude. Specifically, the increase in anodic reaction is more remarkable in comparison with the cathodic reaction due to destruction of passive films under high cavitation intensities; thus, E_{corr} exhibits obvious decline (Point C in Figure 5b) compared with the static case (Point A in Figure 5b). Furthermore, E_{corr} at a high cavitation intensity corresponding to 55 μm CE amplitude shows a similar change (Point D in Figure 5b) when compared to the case with 25 μm CE amplitude.

3.4. Potentiostatic Polarization Curves under Different Cavitation Intensities

Figure 6a illustrates potentiostatic polarization of 316L SS at different CE amplitudes under alternating CE and quiescence states. It is obvious that current density of all samples increases when CE begins and that the value of current density becomes larger with an increase in CE amplitude, indicating faster corrosion rates. However, the current density shows a rapid decline when CE is switched off, which is attributed to the fast self-repair response due to the superior repassivation performance for 316L SS. It is worth noting that the static current density after 300 s of CE displays an increasing trend with increases in CE amplitude, implying that repassivation gradually decreases with an elevated cavitation intensity. Additionally, it is evident that repair times after each CE–quiescence cycle tends to increase with increased cavitation intensity, which is indicative of deteriorated repassivation performance for 316L SS.

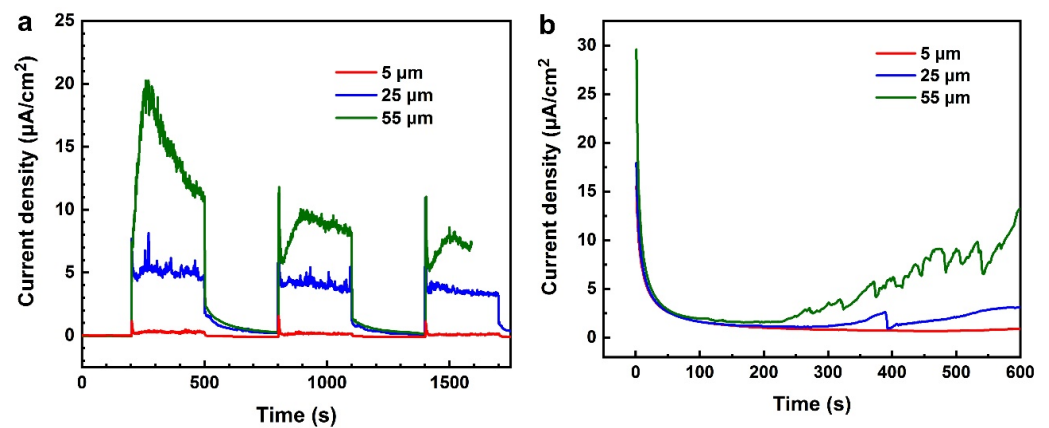


Figure 6. Potentiostatic polarization plots of 316L SS at different CE amplitudes. (a) under alternating CE and quiescence states. (b) static potentiostatic polarization curves after CE for 40 min.

Figure 6b shows static potentiostatic polarization curves after CE for 40 min, and the applied potential is 0 V vs. OCP. The current density with different CE amplitudes shows a rapid decrease when CE is closed, reflecting a self-repairing process of 316L SS during the quiescent state. Current density maintains a stable value of $0.75 \mu\text{A}/\text{cm}^2$ after CE with $5 \mu\text{m}$ amplitude, implying that low CE amplitudes have little effects on the protection of passive films. In contrast, current densities with CE amplitudes of $25 \mu\text{m}$ and $55 \mu\text{m}$ are about $2.95 \mu\text{A}/\text{cm}^2$ and $10.13 \mu\text{A}/\text{cm}^2$, respectively, after 600 s' test, which reflects weak repassivation ability. Taken together, repassivation properties of 316L SS gradually weakened with increased cavitation intensity.

3.5. Passive Film Stability of 316L SS after CE with Different Amplitudes

In order to evaluate the protection of passive films formed on samples with different CE amplitudes, Mott–Schottky plots were obtained, as shown in Figure 7. It should be noted that Mott–Schottky tests are carried out in the static state because they are sensitive to changes in the surroundings. It is clear that the slopes of Mott–Schottky curves under the three amplitudes are positive; that is, the passive films formed on 316L SS under the three types of CE amplitudes exhibit characteristics of *n*-type semiconductors. According to the Mott–Schottky equation for *n*-type semiconductors, some important parameters can be obtained [43]:

$$C_{\text{sc}}^{-2} = \frac{2}{\epsilon_r \epsilon_0 e N_D} \left(E - E_{\text{FB}} - \frac{kT}{e} \right) \quad (3)$$

where C_{sc} is the space-charge capacitance, ϵ_r represents the dielectric of stainless steels taken as 15.6 [44], ϵ_0 is the vacuum permittivity ($8.845 \times 10^{-14} \text{ F/cm}$), N_D and E are the carrier density in *n*-type passive films and the applied potential (V_{SCE}), respectively, e is electron charge ($1.6 \times 10^{-19} \text{ C}$) and T is the absolute temperature taken as 298 K. In addition, E_{FB} and k represent the flat-band potential (V_{SCE}) and Boltzmann constant ($1.38 \times 10^{-23} \text{ J/K}$), respectively. K_{slope} can be obtained by linearly fitting the slope of the Mott–Schottky curve in order to express the value of N_D as follows.

$$K_{\text{slope}} = \frac{dC^{-2}}{dE} = \frac{2}{\epsilon_r \epsilon_0 e N_D} \quad (4)$$

$$N_D = \frac{2}{\epsilon_r \epsilon_0 e K_{\text{slope}}} \quad (5)$$

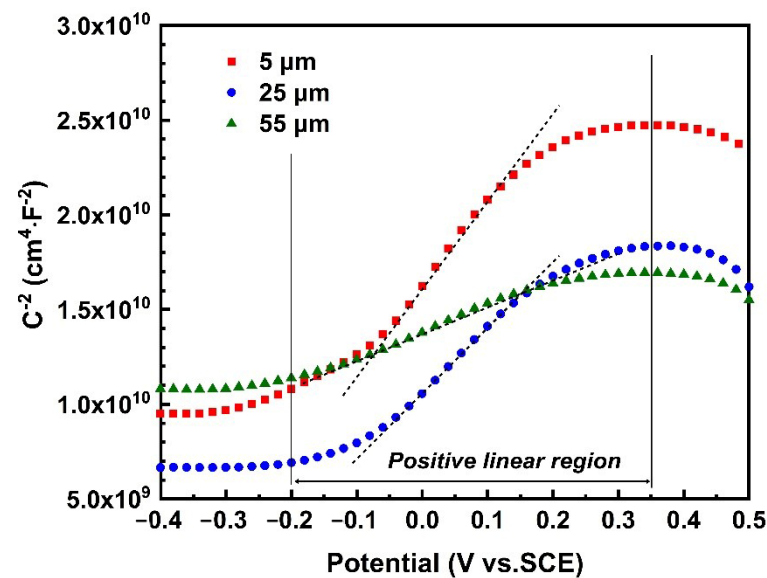


Figure 7. Mott–Schottky plots of 316L SS after 2 h CE with different amplitudes.

As shown in Equation (5), N_D is inversely related to the K_{slope} , which reflects that the greater the slope, the lower the N_D . It can be seen from Figure 7 that the slope of the Mott–Schottky curve decreases when amplitude increases. Furthermore, the fitting parameters of Mott–Schottky plots are shown in Table 3. From the data obtained, all R^2 values are 0.99, indicating a high level of fitting. The conductivity of passive films can be reflected by N_D , with lower N_D meaning higher film resistance and implying better protective capacities of passive films. Obviously, the passive films formed on samples with 5 μm CE amplitude display low N_D ($0.55 \times 10^{21} \text{ cm}^{-3}$), indicating high passive film stability. However, with the increase in CE amplitude, the value of N_D increases to $1.33 \times 10^{21} \text{ cm}^{-3}$ and $2.80 \times 10^{21} \text{ cm}^{-3}$, with CE amplitudes of 25 μm and 55 μm , respectively, indicating reduced passive film stability when CE amplitude increases. In summary, the stability of passive films decreases when CE amplitude increases, resulting in weak protection of passive films with high carrier density.

Table 3. Fitting parameter of Mott–Schottky plots and calculated values of samples with different amplitudes.

Amplitude	$K_{\text{slope}} (\times 10^{10})$	$N_D (\times 10^{21} \text{ cm}^{-3})$	R^2
5 μm	1.651	0.55	0.99
25 μm	0.679	1.33	0.99
55 μm	0.324	2.80	0.99

4. Conclusions

In this research, the effect of cavitation intensity on CE behavior of 316L SS in 3.5 wt.% NaCl solution was investigated, and the major findings are summarized as follows.

(1) Results of OCP indicated that a low cavitation intensity corresponding to a CE amplitude of 5 μm was lower than that of the mechanical bearing capacity of passive films. OCP shifted to the noble direction instantaneously when CE was switched on, and OCP under the CE state still maintained higher values compared with those of the quiescent state, which was mainly attributed to the enhanced oxygen transfer of the cathode due to the stirring effects of CE. In contrast, high cavitation intensities corresponding to CE amplitudes of 25 μm and 55 μm exceeded the mechanical bearing capacities of passive films, causing significantly reduced OCPs compared with the quiescent state. With high cavitation intensities, the passive films of 316L SS were destroyed, and the dissolution of the anode was dominant.

(2) The results of potentiostatic polarization and Mott–Schottky tests showed that 316L SS subjected to low cavitation intensities with a CE amplitude of 5 μm displayed good repassivation properties. However, repassivation performance was markedly weakened when high cavitation intensities corresponding to CE amplitudes of 25 μm or 55 μm were applied, resulting in weak protection of passive films with high carrier densities.

Author Contributions: J.H.: experimental investigation, data analysis and writing. L.Z.: conceptualization and writing—review and editing. A.M.: formal analysis and experimental investigation. P.M.: conceptualization and supervision. Y.Z.: conceptualization and supervision. All authors have read and agreed to the published version of the manuscript.

Funding: This work was supported by the National Natural Science Foundation of China (52101105), Chinese Postdoctoral Science Foundation (2020M670811) and China National Nuclear Corporation (CNNC) Science Fund for Talented Young Scholars.

Data Availability Statement: Raw and processed data are available from L.Z. (Email: lmzhang14s@imr.ac.cn) upon reasonable request.

Conflicts of Interest: The authors declare no conflict of interest.

References

1. Hanke, S.; Fischer, A.; Beyer, M.; dos Santos, J. Cavitation erosion of NiAl-bronze layers generated by friction surfacing. *Wear* **2011**, *273*, 32–37. [[CrossRef](#)]
2. Lavigne, S.; Pougoum, F.; Savoie, S.; Martinu, L.; Klemberg-Sapieha, J.E.; Schulz, R. Cavitation erosion behavior of HVOF CaviTec coatings. *Wear* **2017**, *386–387*, 90–98. [[CrossRef](#)]
3. Zhang, H.; Chen, X.; Gong, Y.; Tian, Y.; McDonald, A.; Li, H. In-situ SEM observations of ultrasonic cavitation erosion behavior of HVOF-sprayed coatings. *Ultrason. Sonochem.* **2019**, *60*, 104760. [[CrossRef](#)] [[PubMed](#)]
4. Nair, R.B.; Arora, H.S.; Grewal, H.S. Microwave synthesized complex concentrated alloy coatings: Plausible solution to cavitation induced erosion-corrosion. *Ultrason. Sonochem.* **2019**, *50*, 114–125. [[CrossRef](#)] [[PubMed](#)]
5. Qiao, L.; Wu, Y.; Hong, S.; Zhang, J.; Shi, W.; Zheng, Y. Relationships between spray parameters, microstructures and ultrasonic cavitation erosion behavior of HVOF sprayed Fe-based amorphous/nanocrystalline coatings. *Ultrason. Sonochem.* **2017**, *39*, 39–46. [[CrossRef](#)] [[PubMed](#)]
6. Zheng, W.; Wu, Y.; Hong, S.; Cheng, J.; Qiao, L.; Cheng, J.; Zhu, S. Electrochemical properties and cavitation erosion behaviors of HVOF sprayed (AlCoCrFeNi)_{1-x}(WC-10Co)_x composite coatings in NaCl medium. *Ceram. Int.* **2021**, *47*, 29410–29422. [[CrossRef](#)]
7. Amann, T.; Waidele, M.; Kailer, A. Analysis of mechanical and chemical mechanisms on cavitation erosion-corrosion of steels in salt water using electrochemical methods. *Tribol. Int.* **2018**, *124*, 238–246. [[CrossRef](#)]
8. Yong, X.; Li, D.; Shen, H. Electrochemical responses to degradation of the surface layer nano-mechanical properties of stainless steels under cavitation. *Mater. Chem. Phys.* **2013**, *139*, 290–297. [[CrossRef](#)]
9. Keswani, M.; Raghavan, S.; Deymier, P. A novel way of detecting transient cavitation near a solid surface during megasonic cleaning using electrochemical impedance spectroscopy. *Microelectron. Eng.* **2013**, *108*, 11–15. [[CrossRef](#)]
10. Ren, X.D.; He, H.; Tong, Y.Q.; Ren, Y.P.; Yuan, S.Q.; Liu, R.; Zuo, C.Y.; Wu, K.; Sui, S.; Wang, D.S. Experimental investigation on dynamic characteristics and strengthening mechanism of laser-induced cavitation bubbles. *Ultrason. Sonochem.* **2016**, *32*, 218–223. [[CrossRef](#)]
11. Ma, X.; Huang, B.; Zhao, X.; Wang, Y.; Chang, Q.; Qiu, S.; Fu, X.; Wang, G. Comparisons of spark-charge bubble dynamics near the elastic and rigid boundaries. *Ultrason. Sonochem.* **2018**, *43*, 80–90. [[CrossRef](#)]
12. Li, D.G.; Wang, J.D.; Chen, D.R.; Liang, P. Influence of passive potential on the electronic property of the passive film formed on Ti in 0.1 M HCl solution during ultrasonic cavitation. *Ultrason. Sonochem.* **2016**, *29*, 48–54. [[CrossRef](#)]
13. Peng, S.; Xu, J.; Jiang, S.; Xie, Z.-H.; Munroe, P. Unlocking the cavitation erosion-corrosion resistance of a TiCN nanocrystalline coating with an equiaxed grain structure. *Corros. Sci.* **2022**, *195*, 109978. [[CrossRef](#)]
14. Wang, Y.; Hao, E.; Zhao, X.; Xue, Y.; An, Y.; Zhou, H. Effect of microstructure evolution of Ti6Al4V alloy on its cavitation erosion and corrosion resistance in artificial seawater. *J. Mater. Sci. Technol.* **2022**, *100*, 169–181. [[CrossRef](#)]
15. García-García, D.M.; García-Antón, J.; Igual-Muñoz, A. Influence of cavitation on the passive behavior of duplex stainless steels in aqueous LiBr solutions. *Corros. Sci.* **2008**, *50*, 2560–2571. [[CrossRef](#)]
16. Li, C.; Zhu, R.; Zhang, X.; Huang, P.; Wang, X.; Wang, X. Impact of surface ultrasonic rolling on cavitation erosion behavior of 304 stainless steel. *Surf. Coat. Technol.* **2020**, *383*, 125280. [[CrossRef](#)]
17. Fernández-Domene, R.M.; Blasco-Tamarit, E.; García-García, D.M.; García-Antón, J. Cavitation corrosion and repassivation kinetics of titanium in a heavy brine LiBr solution evaluated by using electrochemical techniques and Confocal Laser Scanning Microscopy. *Electrochim. Acta* **2011**, *58*, 264–275. [[CrossRef](#)]

18. Fernández-Domene, R.M.; Blasco-Tamarit, E.; García-García, D.M.; García-Antón, J. Repassivation of the damage generated by cavitation on UNS N08031 in a LiBr solution by means of electrochemical techniques and confocal laser scanning microscopy. *Corros. Sci.* **2010**, *52*, 3453–3464. [[CrossRef](#)]
19. Kwok, C.T.; Cheng, F.T.; Man, H.C.; Ding, W.H. Corrosion characteristics of nanostructures layer on 316L stainless steel fabricated by cavitation-annealing. *Mater. Lett.* **2006**, *60*, 2419–2422. [[CrossRef](#)]
20. Li, D.G.; Wang, J.D.; Chen, D.R.; Liang, P. The role of passive potential in ultrasonic cavitation erosion of titanium in 1 M HCl solution. *Ultrason. Sonochem.* **2016**, *29*, 279–287. [[CrossRef](#)]
21. Zhao, G.; Cao, L.; Che, B.; Wu, R.; Yang, S.; Wu, D. Towards the control of blade cavitation in a waterjet pump with inlet guide vanes: Passive control by obstacles. *Ocean Eng.* **2021**, *231*, 108820. [[CrossRef](#)]
22. Paolantonio, M.; Hanke, S. Damage mechanisms in cavitation erosion of nitrogen-containing austenitic steels in 3.5% NaCl solution. *Wear* **2021**, *464–465*, 203526. [[CrossRef](#)]
23. Zheng, Y.; Luo, S.; Ke, W. Effect of passivity on electrochemical corrosion behavior of alloys during cavitation in aqueous solutions. *Wear* **2007**, *262*, 1308–1314. [[CrossRef](#)]
24. Niederhofer, P.; Huth, S. Cavitation erosion resistance of high interstitial CrMnCN austenitic stainless steels. *Wear* **2013**, *301*, 457–466. [[CrossRef](#)]
25. Wang, K.Y.; Lo, K.H.; Kwok, C.T.; Wong, M.M.; Iong, I.W.; Ai, W. The influences of martensitic transformations on cavitation-erosion damage initiation and pitting resistance of a lean austenitic stainless steel. *Mater. Res.* **2016**, *19*, 1366–1371. [[CrossRef](#)]
26. Zhang, R.; Shen, H.; Zhang, Y.; Li, D.; Li, Y.; Yong, X. Surface layer nano-mechanical responses to interaction between cavitation and electrochemical corrosion. *Acta Metall. Sin.* **2013**, *49*, 614–620. [[CrossRef](#)]
27. Luo, S.Z.; Zheng, Y.G.; Li, M.C.; Yao, Z.M.; Ke, W. Effect of cavitation on corrosion behavior of 20SiMn low-alloy steel in 3% sodium chloride solution. *Corrosion* **2003**, *59*, 597–605. [[CrossRef](#)]
28. Kwok, C.T.; Cheng, F.; Man, H. Synergistic effect of cavitation erosion and corrosion of various engineering alloys in 3.5% NaCl solution. *Mater. Sci. Eng. A* **2000**, *290*, 145–154. [[CrossRef](#)]
29. Kim, S.-J.; Lee, S.-J.; Chong, S.-O. Electrochemical characteristics under cavitation-erosion for STS 316L in seawater. *Mater. Res. Bull.* **2014**, *58*, 244–247. [[CrossRef](#)]
30. Bahrami, A.; Mousavi Anijdan, S.H.; Golozar, M.A.; Shamanian, M.; Varahram, N. Effects of conventional heat treatment on wear resistance of AISI H13 tool steel. *Wear* **2005**, *258*, 846–851. [[CrossRef](#)]
31. Nair, R.B.; Arora, H.S.; Mukherjee, S.; Singh, S.; Singh, H.; Grewal, H.S. Exceptionally high cavitation erosion and corrosion resistance of a high entropy alloy. *Ultrason. Sonochem.* **2018**, *41*, 252–260. [[CrossRef](#)]
32. G32-10 A.; Standard Test Method for Cavitation Erosion Using Vibratory Apparatus. ASTM Int.: West Conshohocken, PA, USA, 2010.
33. Li, Z.X.; Zhang, L.M.; Ma, A.L.; Hu, J.X.; Zhang, S.; Daniel, E.F.; Zheng, Y.G. Comparative study on the cavitation erosion behavior of two different rolling surfaces on 304 stainless steel. *Tribol. Int.* **2021**, *159*, 106994. [[CrossRef](#)]
34. Zheng, Z.-B.; Long, J.; Guo, Y.; Li, H.; Zheng, K.-H.; Qiao, Y.-X. Corrosion and impact-abrasion-corrosion behaviors of quenching-tempering martensitic Fe–Cr alloy steels. *J. Iron Steel Res. Int.* **2022**. [[CrossRef](#)]
35. Song, Q.N.; Tong, Y.; Li, H.L.; Zhang, H.N.; Xu, N.; Zhang, G.Y.; Bao, Y.F.; Liu, W.; Liu, Z.G.; Qiao, Y.X. Corrosion and cavitation erosion resistance enhancement of cast Ni–Al bronze by laser surface melting. *J. Iron Steel Res. Int.* **2021**. [[CrossRef](#)]
36. Chen, Z.X.; Hu, H.X.; Zheng, Y.G.; Guo, X.M. Effect of groove microstructure on slurry erosion in the liquid-solid two-phase flow. *Wear* **2021**, *466*, 203561. [[CrossRef](#)]
37. Qiao, Y.; Wang, X.; Yang, L.; Wang, X.; Chen, J.; Wang, Z.; Zhou, H.; Zou, J.; Wang, F. Effect of aging treatment on microstructure and corrosion behavior of a Fe–18Cr–15Mn–0.66N stainless steel. *J. Mater. Sci. Technol.* **2022**, *107*, 197–206. [[CrossRef](#)]
38. Li, Z.X.; Zhang, L.M.; Udoh, I.I.; Ma, A.L.; Zheng, Y.G. Deformation-induced martensite in 304 stainless steel during cavitation erosion: Effect on passive film stability and the interaction between cavitation erosion and corrosion. *Tribol. Int.* **2022**, *167*, 107422. [[CrossRef](#)]
39. Zhang, L.M.; Li, Z.X.; Hu, J.X.; Ma, A.L.; Zhang, S.; Daniel, E.F.; Umoh, A.J.; Hu, H.X.; Zheng, Y.G. Understanding the roles of deformation-induced martensite of 304 stainless steel in different stages of cavitation erosion. *Tribol. Int.* **2021**, *155*, 106752. [[CrossRef](#)]
40. Wang, Z.B.; Zheng, Y.G. Critical flow velocity phenomenon in erosion-corrosion of pipelines: Determination methods, mechanisms and applications. *J. Pipeline Sci. Eng.* **2021**, *1*, 63–73. [[CrossRef](#)]
41. Bakhshandeh, H.R.; Allahkaram, S.R.; Zabihi, A.H. An investigation on cavitation-corrosion behavior of Ni/ β -SiC nanocomposite coatings under ultrasonic field. *Ultrason. Sonochem.* **2019**, *56*, 229–239. [[CrossRef](#)]
42. Xu, J.; Peng, S.; Li, Z.; Jiang, S.; Xie, Z.-H.; Munroe, P. The influence of semiconducting properties of passive film on the cavitation erosion resistance of a NbN nanoceramic coating. *Ultrason. Sonochem.* **2021**, *71*, 105406. [[CrossRef](#)] [[PubMed](#)]
43. Zhang, L.M.; Zhang, S.D.; Ma, A.L.; Umoh, A.J.; Hu, H.X.; Zheng, Y.G.; Yang, B.J.; Wang, J.Q. Influence of cerium content on the corrosion behavior of Al–Co–Ce amorphous alloys in 0.6 M NaCl solution. *J. Mater. Sci. Technol.* **2019**, *35*, 1378–1387. [[CrossRef](#)]
44. Wang, B.-C.; Zhu, J.-H. Influence of ultrasonic cavitation on passive film of stainless steel. *Ultrason. Sonochem.* **2008**, *15*, 239–243. [[CrossRef](#)] [[PubMed](#)]